Millimeter and terahertz detectors based on plasmon excitation in InGaAs/InP HEMT devices.

Nima Nader Esfahani*[a,b], Robert E. Peale[a], Walter R. Buchwald[b,c], Joshua R. Hendrickson[d] and Justin W. Cleary[d]
[a]Department of Physics, University of Central Florida, Orlando FL, USA 32816
[b]Solid State Scientific Corporation, Nashua, NH 03060
[c]Department of Physics, University of Massachusetts, Boston, Boston MA, USA 02125
[d]Air Force Research Laboratory, Sensors Directorate, Wright Patterson AFB OH 45433

ABSTRACT

Recent progress in the investigation of millimeter-wave and THz detectors based on plasmon excitation in the two-dimensional electron gas (2DEG) of a high electron mobility transistor (HEMT) is reported. A tunable resonant polarized photoresponse to mm-wave radiation in the frequency range of 40 to 110 GHz is demonstrated for a grating-gated InGaAs/InP based device. The gate consisted of a metal grating with period of 9 μm specifically designed for excitation of sub-THz plasmons. The resonant excitation of plasmons, which shifts with gate-bias, changes the channel conductance. This resonant change in channel conductance enables potential applications in chip-scale frequency-agile detectors, which can be scaled to mid-THz frequencies.

Keywords: HEMT, Plasmon, terahertz, Graphene, 2DEG, detector

1. INTRODUCTION

The excitation of plasmons in the two-dimensional electron gas (2DEG) is an established phenomenon for a number of material systems which includes Si-inversion layers [1], GaAs Field effect transistors (FETs) [2-5], InGaAs/InP HEMTs [6,7], and GaN HEMTs [8]. A coupling structure, such as a grating [1-4, and 6] or antenna [5], is required to match momentum between free space radiation and plasmon modes. The resonance frequency of the plasmon is dependent on the 2DEG sheet charge density, which in turn depends on the external gate-voltage, V_g, applied to the metallized grating. This provides a means to actively tune plasmon modes over a wide range of frequencies. In some cases, plasmon excitation has been observed to give rise to a change in channel conductance [2-5, and 9]. In the device investigated here, the grating also doubles as a gate, which allows for the tuning of the plasmon absorption frequency because of the dependence of the plasmon dispersion relation on sheet charge density. This tunable electrical photoresponse provides a basis for on-chip sub-THz and THz spectral detection.

The InGaAs/InP materials system benefits from high sheet charge density, large mobility, and low electron effective mass, which results in theoretically sharp plasmon resonances up to mid-THz frequencies. This work presents first reports of polarized resonant photoresponse for this material system at millimeter wavelengths, where the availability of stable tunable, modulated sources facilitates the observations. Such resonance behavior can be shifted to THz frequencies by designing grating areas with smaller, sub-micron periods, which we are also investigating using the same material system. However, for the purpose of this paper we focus on investigation of the devices designed for the mm-wave regime.

2. THEORY

The dispersion relation for 2D-plasmons is given by [1]

$$\omega_n{}^2 = \frac{e^2 n_s q_n}{m^* \epsilon_0}\left(\varepsilon_b + \varepsilon_t coth(q_n d)\right)^{-1}, \quad (1)$$

where ω_n is the frequency of the nth integer order plasmon, e the electron charge, m^* the effective mass, d the 2DEG depth from the grating, n_s the 2DEG sheet charge density, and ε_t (ε_b) are the relative permittivity of the semiconductor layers on top of (beneath) the 2DEG, respectively. The allowed plasmon wavevector, q_n, takes discrete values $2\pi n/a$, and generally exceeds the wavevector of the external radiation, which accounts for the momentum mismatch.

The transmittance spectra can be calculated for different gate biases following the approach discussed in the theory of 2D-grating couplers [6, 10, and 11]. Device parameters needed as inputs are sheet charge density, n_s, and relaxation time, τ, which can be determined from measured temperature dependent Source-Drain I-V curves. To estimate these values, formulas in [12] are fitted to the values of saturated Source-Drain current, $I_{sd\text{-sat}}$, at different gate voltages, V_g, to find, as fitting parameters the mobility, μ, and the temperature dependent carrier concentration in the absence of a quantum well, n_d. The latter is used to determine τ and n_s as a function of applied V_g.

The method used to interpret the experimental response in terms of calculated transmittance is same as the one explained in [9], with one minor difference. In this report, the final relation lacks an experimental scaling factor due to a change in the data recording process, giving the relation between experimental results and theoretical calculations as

$$V_{out}(V_g, f) = \frac{2}{\pi} BW \left(\frac{-dT(v_g,f)}{df}\right) R_L \Delta f \ . \quad (2)$$

In Eq. (2), V_{out} is the output of lock-in amplifier, and B is an unknown coupling factor between plasmon absorption and measured photoresponse and is assumed to be both frequency independent and gate-bias dependent. W is the effective radiation power transferred to the 2DEG at each frequency, R_L is the load resistor at the Drain of the device, Δf is the amplitude of frequency modulation in the mm-wave source and dT/df is the derivative of the calculated transmittance spectrum of the device with respect to frequency.

3. EXPERIMENTAL DETAILS

In contrast with Ref [6], we selected a HEMT structure with two δ-doped layers, which transfer charge to the 2DEG. This avoids any anomalous, free carrier induced effects [13]. A grating-gate with period, a, of 9 μm and t/a = 0.22, where t is the width of the opening between grating bars, was chosen so that the fundamental plasmon resonance is expected to be near 9 cm^{-1}. Figure 1 presents the device layer structure.

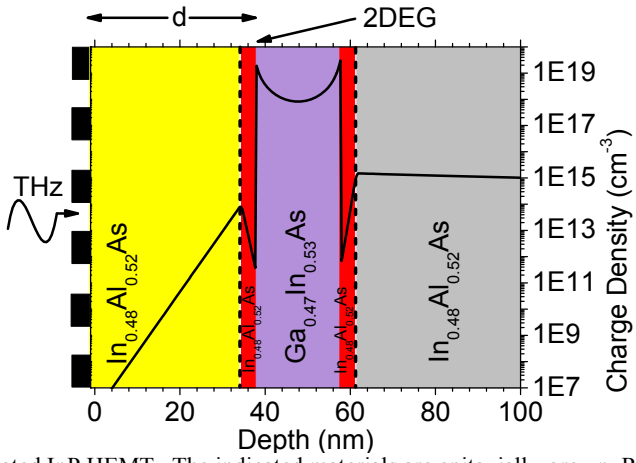

Figure 1. Schematic of grating-gated InP HEMT. The indicated materials are epitaxially-grown. Radiation is incident on the grating-gate from the left. The black curve indicates the calculated charge density distribution.

Ohmic contacts of Ge/Au were used to form the Source and Drain contact pads. For gate formation, the doped-InGaAs cap layer of the molecular beam epitaxially grown InGaAs/InP structure was first removed and a 20 nm Ti layer was deposited on top of gate region with an area of 195 μm x 250 μm. An Au grating of 9 μm period and openings of width t

that are 22% of the period was patterned by e-beam lithography over the entire gate region. The gate metal deposited consists of 15 nm of Ti and 100 nm of Au. Source, Gate, and Drain bond pads were fabricated by photolithography using 50 nm of Ti followed by 250 nm of Au. The sample was mounted in a traditional transistor package. An optical picture of the device is presented in figure 2 (left) with a SEM picture of grating area presented in figure 2 (Right).

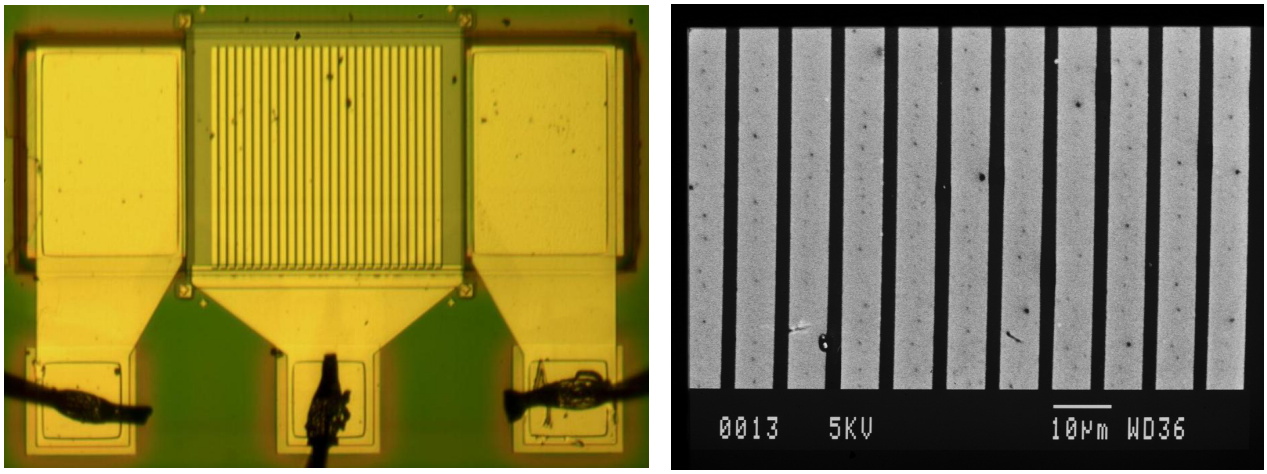

Figure 2. (left) Optical microscope image of grating gated InP-based HEMT. The gate dimensions are 195 µm x 250 µm**. (right)** A SEM picture of the metal grating with 9 µm period and t/a =0.22.

During the experiments, the sample temperature was maintained at 4 K. Two backward wave oscillator (BWO) heads with frequency ranges of 40 - 60 GHz and 83 - 108 GHz generated the mm-wave radiation. Resonant photoresponse of the device was monitored using a lock-in amplifier while the frequency of the radiation was modulated with modulation amplitude of Δf. This experimental setup was the same as in [9]; however, in contrast the lock-in amplifier was connected to the same laptop that was used to run the rest of the setup through a GPIB port. This enabled us to control the lock-in and directly record experimental data through the GPIB connection, which reduced the number of electronic devices and improved the signal-to-noise ratio.

An experimental setup was also designed to test the polarization of sub-THz radiation which consisted of two gain horns placed in front of each other. They are referred to as the emitting and collecting horns, respectively. The emitted mm-wave radiation generated by the BWO propagates through free space before being collected by the collecting horn for detection by a crystal detector. The emitting horn was fixed throughout the experiment with a vertical polarization axis. The collecting horn was rotatable about the optical axis so that its polarization axis could be either horizontal or vertical. Figure 3 shows a schematic of the setup in a case where polarization axes were oriented perpendicular to each other. In this figure the electric field exiting the emitting horn with vertical polarization is labeled with E_1 while the field collected on the right is called E_2.

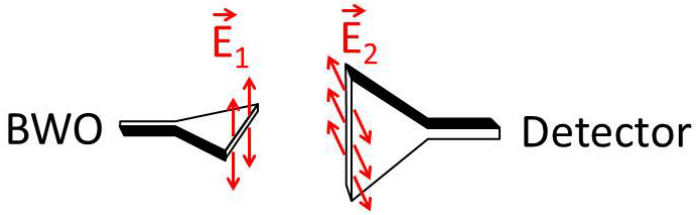

Figure 3. Schematic of the experimental setup used to study the polarization of the incident sub-THz radiation. Two gain horns are illustrated in the case that their polarization axes are perpendicular to each other.

4. RESULTS

Source-Drain IV-measurements were completed as a function of gate-bias in order to determine n_s and τ of the device. Data taken at 4 K sample temperature for V_g between 0 to -0.5 V with steps size of -0.1 V are presented in figure 4 (left).

Source-Drain current, I_{SD}, saturates at V_{SD} in the range of 1 to 1.5 V to different levels which decrease with increasing negative gate bias until the HEMT reaches pinch off at around V_g = -0.6 V.

The $I_{sd,sat}$ data at 4 K are plotted in figure 4 (right) as a function of gate voltage with red colored symbols while the black curve is a fit of formulas from [12] to the data. The fit parameters n_d and μ, also show in the figure, allow determination of relaxation time to be 0.37 ps and sheet charge densities, n_s, to be 1.39, 1.21, and 1.04 x 10^{12} cm^{-2} at gate biases of 0, -0.1, and -0.2 V, respectively.

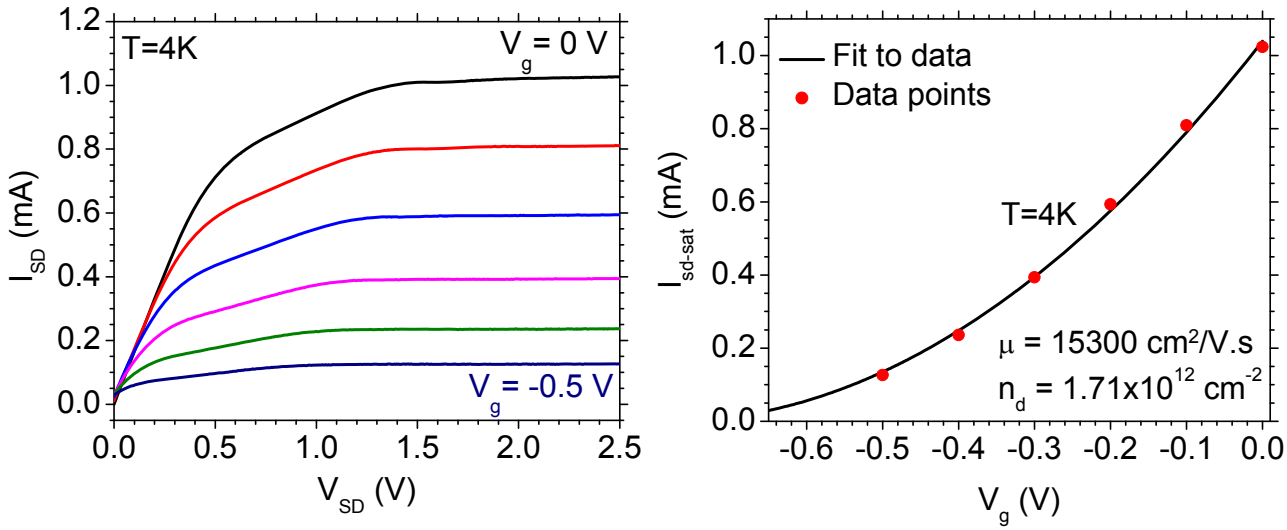

Figure 4 (left). Measured IV-Curves of the device at T = 4K. **(Right)** I_{sd-sat} vs V_g data (symbols) and fits (lines). Values of fitting parameters are also shown.

Figure 5 (top) presents the calculated device transmittance spectra at 4 K for frequencies up to 500 GHz. Calculated spectra for gate-biases of 0, -0.1, and -0.2 V are shown with black, red and blue curves, respectively. The figure pictorially represents approximately the low frequency half of the plasmon resonances since they tend to be very broad in the sub-THz region. Peak absorption occurs at 365, 340 and 320 GHz for V_g = 0, -0.1, and -0.2 V, respectively, as indicated by symbols. This shows a redshift with increasing negative V_g and thus decreasing n_s, which is in agreement with Eq. 1. The absorption band also becomes shallower, which is reasonable since electrons are required for plasmon absorption and increasing the negative gate-bias results in the reduction of the 2DEG free carrier concentration.

Figure 5 (bottom) presents the slope of the transmittance spectra with respect to frequency, *dT/df*. During the photoresponse measurements, the lock-in output is proportional to the slope of the transmittance spectrum, (see Eq. 2), therefore, these curves will be utilized to compare theory to experiment. Two horizontal bars indicate the tuning ranges of two BWO sources, which fall near the low-frequency side of the resonance with a significant *dT/df*. Minima of plasmon absorption lines are marked by symbols with colors and they point to the frequencies at which the derivative curves pass zero.

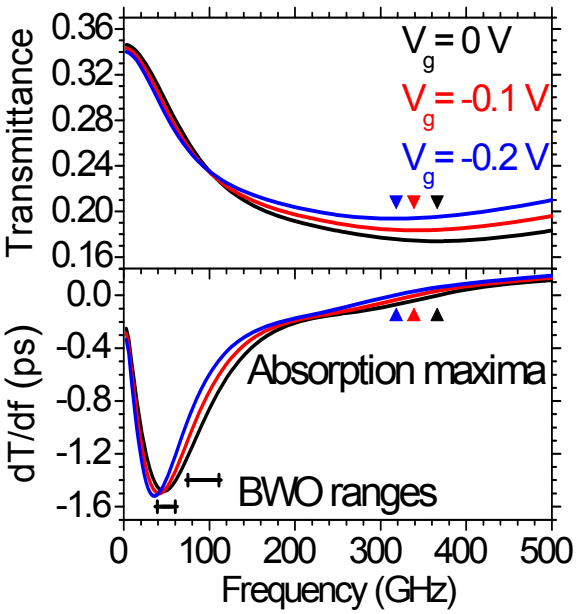

Figure 5. (Top) Calculated transmittance spectra in the range of 0-500 GHz. Absorption maxima for three different gate biases are marked with symbols. **(Bottom)** Calculated *dT/df* spectra in the same frequency range. The horizontal bar indicates our BWO range.

The measured photoresponse of the device is shown in figure 6 for gate-biases of 0, -0.1, and -0.2 V with black, red and blue curves, respectively. The effect is measured in two frequency ranges of 40 to 60 GHz and 83 to 108 GHz and for two nominal radiation polarizations, which were intended to be perpendicular and parallel to the gratings direction. During the measurement, the incident power, *W,* was kept constant over the entire frequency range. Figures 6 (a) and (b) show the photoresponse to the incident radiation with a nominal perpendicular polarization over the frequency ranges of 40-60 GHz and 83-108 GHz, respectively while figures 6 (c) and (d) show the same effect over the same frequency ranges but with the radiation polarization parallel to the grating strips. Also shown in figure 6 are linear fits to the measured data, which represent the average photoresponse and frequency dependence for each V_g.

The detected photoresponse shows sharp features at discrete frequencies as opposed to an expected continuous electrical response. This is an experimental artifact common to mm-wave spectroscopy and is caused by field interference and the formation of standing waves. When standing wave nodes occur at the grating, no power is transferred to the plasmons and no electrical response will be detected, while at frequencies at which anti-nodes occur, coupling to plasmons and a corresponding electrical response may occur.

As mentioned earlier, the gain horn was oriented in such a way to produce an electric field with either perpendicular or parallel polarization relative to the gating strips. The proper orientations of the gain horn for such polarizations are illustrated in the insets of figures 6 (b) and (d), respectively. No plasmon excitation was expected for parallel polarization because such polarization does not polarize the grating stripes and produce the local fields required to excite a plasmon resonance. As seen in figure 6 however, a photoresponse was observed for both polarization cases, although the response appears somewhat weaker in the parallel case.

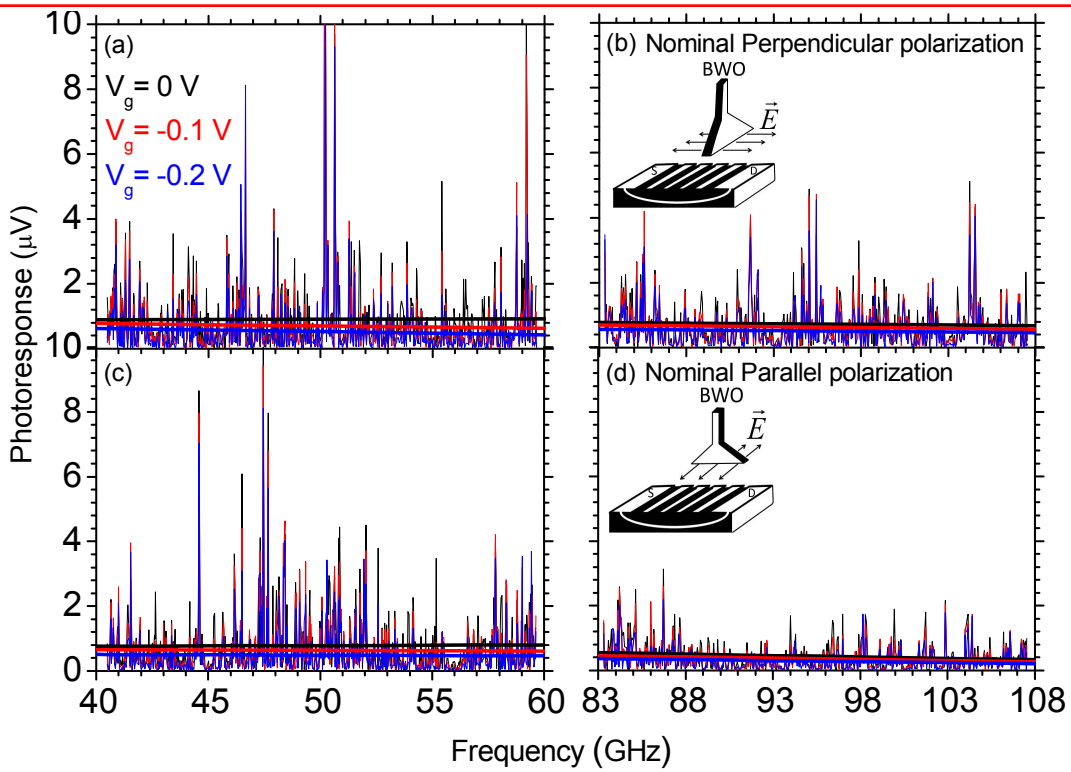

Figure 6. Photoresponse of the HEMT at T = 4 K to mm-wave radiation for three gate biases. **(a)** For perpendicular polarization in frequency range of 40-60 GHz. **(b)** For perpendicular polarization in frequency range of 83-108 GHz **(c)** For parallel polarization in frequency range of 40-60 GHz. **(d)** For parallel polarization in frequency range of 83-108 GHz. Straight lines are linear fits that represent an average over the apparent standing wave effects. The indicated polarizations were the nominal ones expected from the horn.

To investigate the unexpected photoresponse for parallel polarization, the experimental setup in figure 3 was used. Figure 7 (left) presents the radiation spectral intensity recorded by a crystal detector when the polarization axes of emitting and collecting horns are aligned for optimum collection. When a wire grid polarizer is placed in the radiation path with wires oriented perpendicular to the beam polarization, the beam is unaffected as anticipated. When the polarizer is rotated 90 degrees, the beam is strongly blocked, also as anticipated.

Figure 7 (right) presents the recorded intensity when the collecting horn is rotated 90 degrees, and illustrates poor radiation detection as anticipated. When the polyethylene cryostat window [9] is placed between the crossed horns, however, a jump in the signal is observed at the higher frequencies. This is attributed to rotation of the polarization by some small angle due to scattering from imperfections in or on the window. A mass of randomly oriented wires produces an even stronger response, suggesting that random reflections from metal surfaces inside the cryostat may also serve to randomly alter the incident polarization. These results explain how the unexpected photoresponse for nominally parallel polarization can arise.

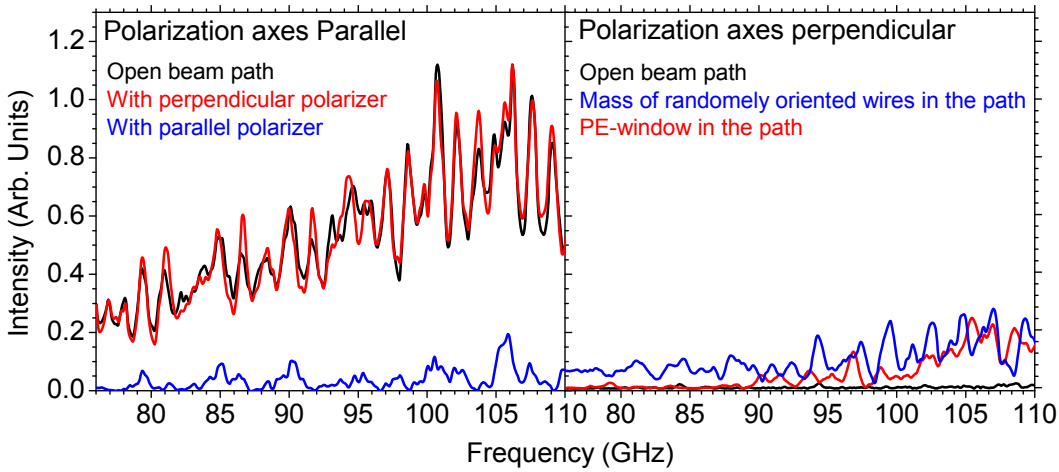

Figure 7. Radiation intensity collected by the collecting horn, radiation power is not leveled. **(Right)** when polarization axes of two horns are parallel **(Left)** when polarization axes are perpendicular.

In figure 6, plotted linear fits represent an average over the photoresponse fluctuations caused by standing waves. Figure 8 compares these lines to the theoretical expectations from figure 5. Both nominal polarizations are compared with theory since the experimental polarization state is impure due to effects demonstrated in figure 7. In figure 8 the data fits for each V_g are vertically scaled to their corresponding calculated values at the center frequency of the plots. Since the coupling factor, B, in Eq. 2 may depend on the applied gate-bias, different scaling factors are used for each data fit.

Data fits in both nominal polarizations are in qualitative agreement with theoretically calculated *dT/df* spectra in a number of significant ways. In both frequency ranges the experimental *dT/df* data decrease monotonically with increasing negative V_g. In the high frequency range, for a given V_g, the *dT/df* data increase monotonically with frequency. In the lower frequency range, for $V_g = 0$, there is significant positive curvature to the theoretical *dT/df* vs. *f* curves, which of course is not reflected in the linear fit to the data points.

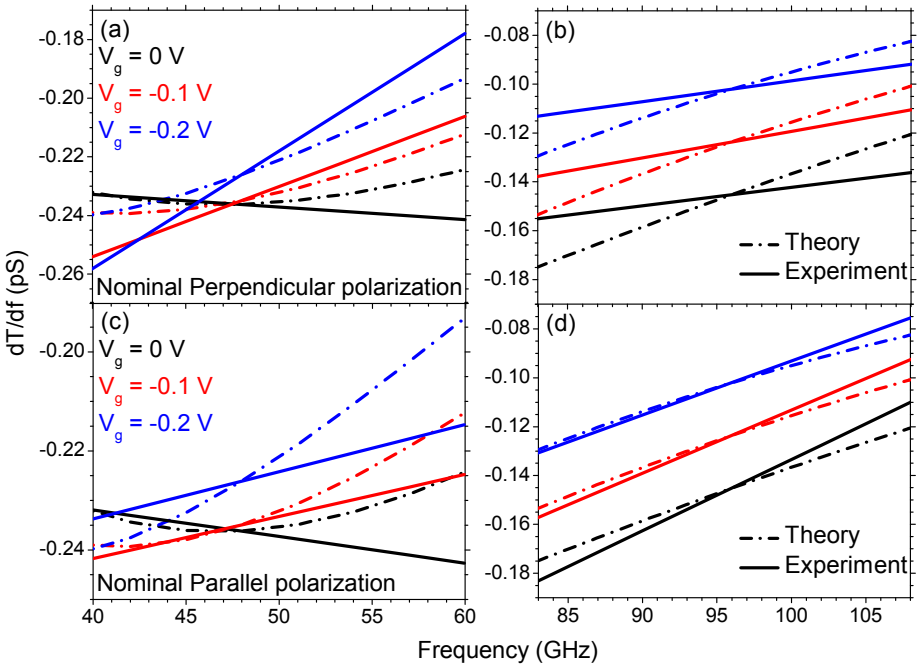

Figure 8. Comparison of theoretical dT/df curves with linear fits to measured photoresponse data. **(a)** nominal perpendicular polarization and in frequency range 40-60 GHz. **(b)** nominal perpendicular polarization and frequency range 83-108 GHz. **(c)** with nominal parallel polarization and frequency range 40-60 GHz. **(d)** Nominal parallel polarization and frequency range 83-108 GHz.

5. SUMMARY

An electrical photoresponse that can be attributed to tunable resonant absorption of mm-wave radiation by 2D-plasmons in the channel of a HEMT has been observed in InGaAs/InP materials system. Experimental observations agree with theory in a number of significant ways, supporting the interpretation of resonant absorption due to plasmon excitation. Namely, in the higher frequency range the experimental *dT/df* data decreases with increasing negative V_g and increasing frequency. In the lower frequency range, measured photoresponse decreases with increasing frequency for gate biases of -0.1 and -0.2 V, however, for $V_g = 0$ V, there is significant positive curvature to the theoretical *dT/df* vs. *f* curves, which is of course not reflected in the linear fit to the data points. The experimental polarization dependence is weaker than expected, which is attributed to an experimental artifact whereby the scattering in the cryostat and from metal parts reduces the degree of linear polarization of the beam incident on the sample. Further analysis of experimental data to investigate the mismatch between the expected and observed effects remains to be resolved and will be the focus of further investigations.

6. ACKNOWLEDGMENTS

NNE and JWC would like to acknowledge support from the Air Force Office of Scientific Research (Program Manager Dr. Gernot Pomrenke) under LRIR number 12RY10COR. REP acknowledges support by the Air Force office of Scientific Research (Program Manager Dr. Gernot Pomrenke) under grant number FA95501010030. JRH would also like to acknowledge support from the Air Force Office of Scientific Research (Program Manager Dr. Gernot Pomrenke) under LRIR number 12RY05COR.

REFERENCES

[1] Allen, S. J. Jr., Tsui D. C., and Logan, R. A., "Observation of the Two-Dimensional Plasmon in Silicon Inversion Layers," Phys. Rev. Lett. **38**, 980 (1977).
[2] Shaner, E. A., Lee, M., Wanke, M. C., Grine, A. D., Reno, J. L., and Allen, S. J., " Single-quantum-well grating-gated terahertz plasmon detectors," Appl. Phys. Lett, **87**, 193507 (2005)
[3] Peralta, X. G., Allen, S. J., Wanke, M. C., Harff, N. E., Simmon, J. A., et al., "Terahertz photoconductivity and plasmon modes in double-quantum-well field-effect transistors," Appl. Phys. Lett. **81,** 1627-1629 (2002)
[4] Knap, W., Deng, Y., Rumyantsev, S., Shur, M. S., "Resonant detection of subterahertz and terahertz radiation by plasma waves in submicron field-effect transistors," Appl. Phys. Lett. **81**, 4637-4639 (2002)
[5] Dyer, G. C., Preu, S., Azin, G. R., Mikalopas, J., et al., "Enhanced performance of sub-terahertz detection in a plasmonic cavity," Appl. Phys. Lett. **100**, 083506 (2012)
[6] Saxena, H., Peale, R. E., and Buchwald, W. R., "Tunable two-dimensional Plasmon resonances in an InGaAs/InP HEMT," J. Appli. Phys. **105,** 113101 (2009).
[7] Nader Esfahani, N., Cleary, J. W., Peale, R. E., Buchwald W. R., Fredricksen, C. J., Hendrickson, J. R., Lodge, M. S., Dawson, B. D., and Ishigami, M., "Investigation of plasmonic absorption lines in terahertz InP- and graphene-based grating-gated transistors for tunable THz and mm-wave detection," Proc. SPIE 8261, 14 (2012)**.**
[8] Muravjov, A. V., Veksler, D. B., Popov, V. V., Polischuk, O. V., Pala, N., Hu, X., Gaska, R., Saxena, H., Peale, R. E., and Shur, M. S., "Temperature dependence of plasmonic terahertz absorption in grating-gate gallium-nitride transistor structures," Appl. Phys. Lett. 96, 042105 (2010).
[9] Nader Esfahani, N., Peale, R. E., Buchwald, W. R., Hendrickson, J. R., and Cleary, J. W., "First observation of a plasmon-mediated tunable photoresponse in a grating-gated InGaAs/InP HEMT for millimeter-wave detection," Proc. SPIE 8512, 33 (2012)**.**
[10] Zheng, L., Schaich, W. L., and MacDonald, A. H., "Theory of two-dimensional grating couplers," Phys. Rev. B **41**, 8493 (1990).
[11] Nader Esfahani, N., Peale, R. E., Cleary, J. W., Buchwald, W. R., "Plasmon resonance response to millimeter-waves of grating-gated InGaAs/InP HEMT," Proc. SPIE 8023, 27 (2011)
[12] Grinberg, A. A., and Shur, M. S., "A new analytical model for heterostructure field-effect transistors," J. Appl. Phys. **65**, 2116 (1989).
[13] Cleary, J. W., Peale, R. E., Saxena, H., and Buchwald, W. R., "Investigation of plasmonic resonances in the two-dimensional electron gas of an InGaAs/InP high electron mobility transistor," Proc. SPIE 8023, 80230X (2011)